PERGAMON

International Journal of Heat and Mass Transfer 43 (2000) 687–704

International Journal of HEAT and MASS TRANSFER

www.elsevier.com/locate/ijhmt

The effect of free-floating dendrites and convection on macrosegregation in direct chill cast aluminum alloys Part II: predictions for Al–Cu and Al–Mg alloys

Christopher J. Vreeman [a,*], Frank P. Incropera [b]

[a] *Heat Transfer Laboratory, School of Mechanical Engineering, Purdue University, West Lafayette, IN 47907, USA*
[b] *College of Engineering, University of Notre Dame, Notre Dame, IN 46556, USA*

Received 26 June 1998; received in revised form 18 May 1999

Abstract

In Part I, a binary mixture model of the DC casting process was proposed, that accounts for fluid flow in the melt and mushy zone, as well as in a slurry zone characterized by the transport of solute-depleted, free-floating dendrites. In this paper, the model is applied to the DC casting of Al–4.5 wt% Cu and Al–6.0 wt% Mg billets, and the predicted surface-to-centerline distribution of macrosegregation is consistent with trends observed in DC cast ingots. These trends include the development of negative segregation at the centerline, subsurface solute enriched and depleted regions, and positive segregation at the billet surface. Negative segregation at the centerline increased with an increase in the packing fraction at which free-floating dendrites are presumed to coalesce into a rigid dendritic structure. Likewise, negative segregation at the centerline and positive segregation in the enriched region increased with an increase in the characteristic diameter of the free-floating dendrites.

Keywords: Heat transfer; Continuous casting; Direct chill casting; Binary alloys; Macrosegregation; Natural convection; Fluid flow; Shrinkage; Solidification; Aluminum

1. Introduction

In a companion paper, Vreeman et al. [1] proposed a fully coupled, single-domain, mixture model of the DC casting process to predict and clarify the complex interactions that cause macrosegregation as ingots solidify. The mixture model was developed to account for fluid flow in the melt and mushy zone, as well as the transport of solute-depleted, free-floating dendrites in an intermediate slurry zone, which is believed to have a significant impact on macrosegregation in DC cast ingots [2–4]. In this study, the model is used to simulate the DC casting of 40 cm diameter, Al–4.5 wt% Cu and Al–6.0 wt% Mg billets.

2. Model implementation

2.1. Transport equations

The model detailed in the companion paper [1] simulates solidification in systems with two-phase (solid–

* Corresponding author. Present address: Rocketdyne Propulsion & Power, 6633 Canoga Avenue, MS PA84, Canoga Park, CA 91309-7922, USA. Tel.: +1 818 586 1156; fax: +1 818 586 0159.

E-mail address: christophe.j.vreeman@boeing.com (C.J. Vreeman).

0017-9310/00/$ - see front matter
PII: S0017-9310(99)00175-1

Nomenclature

c	specific heat (J/kg K)
d	characteristic dendrite diameter (μm)
D	mass diffusion coefficient (m^2/s)
f	mass fraction
g	volume fraction, gravitational acceleration (m/s^2)
h	enthalpy, latent heat (J/kg)
k	thermal conductivity (W/m K)
k_p	partition coefficient
K	permeability (m^2)
L	axial length of computational domain (m)
P	reduced pressure (N/m^2)
q''	billet surface heat flux (W/m^2)
r, z	axisymmetric coordinates (m)
R	radius of computational domain (m)
t	time (s)
T	temperature (K)
u	axial velocity component (m/s)
U	overall heat transfer coefficient (W/m^2 K)
v	radial velocity component (m/s)
$\vec{V}$	velocity vector (m/s)
β_S	solutal expansion coefficient
β_T	thermal expansion coefficient (K^{-1})
κ_0	permeability coefficient (m^2)
μ	dynamic viscosity (kg/s m)
ρ	density (kg/m^3)

Subscripts

c	convection sink
eut	eutectic
f	fusion
l	liquid
melt	melting point
0	reference, nominal value
p	packed, rigid structure
s	solid
S	solutal
T	thermal

Superscript

A generic element

liquid) regions consisting of a slurry of free-floating dendrites above a rigid, dendritic matrix saturated with interdendritic liquid (Fig. 1). Mixture transport equations for mass, energy, and species conservation [5] are applied in all regions of the DC cast billet as it solidifies, while the application of separate and distinct momentum equations depends on the local solid morphology [1]. In the liquid and slurry regions, for which the solid volume fraction is less than the designated *packing fraction* ($g_s < g_{s,p}$), modified versions of slurry momentum equations developed by Ni and Incropera [6] are employed (Table 1). In regions consisting of a rigid, solid structure and interdendritic liquid ($g_s \geq g_{s,p}$), momentum equations developed by Bennon and Incropera [5] and Prescott et al. [7] are employed to account for interdendritic fluid flow in a translating solid matrix.

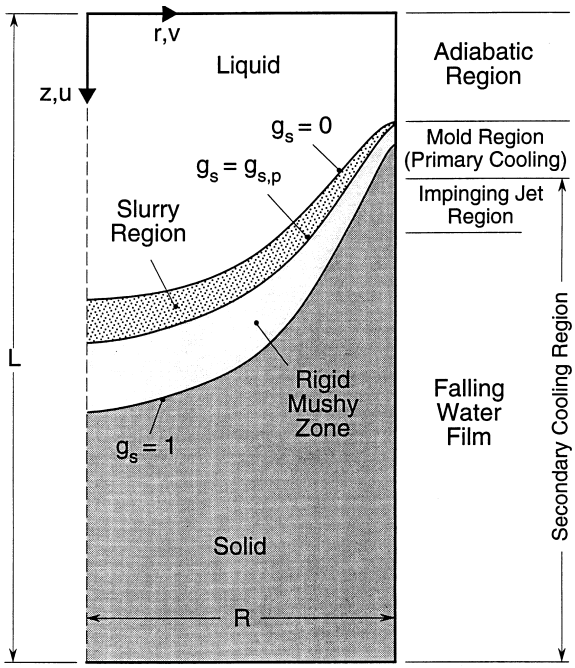

Fig. 1. Axisymmetric computational domain for DC casting of a cylindrical billet.

The parameter that defines the relative extent of the slurry and rigid, mushy zone regions is the packing fraction, $g_{s,p}$, at which the free-floating dendrites coalesce to form a rigid dendritic structure (Fig. 1). In general, packing fractions are not explicitly known and vary significantly from system to system. In addition to the packing fraction, the characteristic diameter of free-floating dendrites, d, used to calculate solid and liquid phase velocity differences [1], is not explicitly known. A rigorous determination of dendrite size variations requires implementation of an additional transport equation and *nucleation model* to account for the advection and 'generation' (through nucleation and/or fragmentation) of dendrites, respectively.

In this study, a parametric investigation is con-

Table 1
Mixture model transport equations

Continuity	$\frac{\partial \rho}{\partial t} + \nabla\left(\rho \vec{V}\right) = 0$
Energy	$\frac{\partial}{\partial t}(\rho h) + \nabla\left(\rho \vec{V} h\right) = \nabla\left(\frac{k}{c_s}\nabla h\right) + \nabla\left(\frac{k}{c_s}\nabla(h_s - h)\right) - \nabla\left(\rho(\vec{V} - \vec{V}_s)(h_l - h)\right)$
Species	$\frac{\partial}{\partial t}(\rho f^A) + \nabla\left(\rho \vec{V} f^A\right) = \nabla(\rho f_l D_l^A \nabla f^A) + \nabla\left(\rho f_l D_l^A \nabla(f^A{}_l - f^A)\right) - \nabla\left(\rho(\vec{V} - \vec{V}_s)(f^A{}_l - f^A)\right)$
	Liquid and slurry regions ($0 \le g_s < g_{s,p}$)
z-Momentum	$\frac{\partial}{\partial t}(\rho u) + \nabla\left(\rho \vec{V} u\right) = \nabla\left(\mu_l \frac{\rho}{\rho_l}\nabla u\right) - \nabla\left(\mu_l \frac{\rho f_s}{\rho_l}\nabla u_s\right) + \nabla(\bar{\mu}_s g_s \nabla u_s) - \nabla\left[\left(\frac{\rho f_s}{f_t}\right)(\vec{V} - \vec{V}_s)(u - u_s)\right]$
	$+ g_s(\rho_s - \rho_l)g - g_s\rho_s g\left[\beta_{T,s}(T - T_0) + \beta_{S,s}(f^A{}_s - f^A_0)\right] - g_l\rho_l g\left[\beta_{T,l}(T - T_0) + \beta_{S,l}(f^A{}_l - f^A_0)\right] - \frac{\partial P}{\partial z}$
r-Momentum	$\frac{\partial}{\partial t}(\rho v) + \nabla\left(\rho \vec{V} v\right) = \nabla\left(\mu_l \frac{\rho}{\rho_l}\nabla v\right) - \mu_l \frac{\rho}{\rho_l}\frac{v}{r^2} - \nabla\left(\mu_l \frac{\rho f_s}{\rho_l}\nabla v\right) + \mu_l \frac{\rho f_s}{\rho_l}\frac{v}{r^2} + \nabla(\bar{\mu}_s g_s \nabla v) - \bar{\mu}_s g_s \frac{v}{r^2} - \frac{\partial P}{\partial r}$
	Rigid mushy zone and solid regions ($g_{s,p} \le g_s \le 1$)
z-Momentum	$\frac{\partial}{\partial t}(\rho u) + \nabla\left(\rho \vec{V} u\right) = \nabla\left(\mu_l \frac{\rho}{\rho_l}\nabla u\right) - \frac{\mu_l}{K}\frac{\rho}{\rho_l}(u - u_s) - \rho_l g\left[\beta_{T,l}(T - T_0) + \beta_{s,l}(f^A{}_l - f^A_0)\right] - \frac{\partial P}{\partial z}$
r-Momentum	$\frac{\partial}{\partial t}(\rho v) + \nabla\left(\rho \vec{V} v\right) = \nabla\left(\mu_l \frac{\rho}{\rho_l}\nabla v\right) - \frac{\mu_l}{K}\frac{\rho}{\rho_l}v - \mu_l \frac{\rho}{\rho_l}\frac{v}{r^2} - \frac{\partial P}{\partial r}$

ducted in which constant values of the packing fraction, $g_{s,p}$, and the characteristic, free-floating dendrite diameter, d, are varied to determine their relative influence on the macrosegregation predicted in Al–4.5 wt% Cu and Al–6.0 wt% Mg billets. In the simulations, consideration is given to packing fractions of 15 and 30% and characteristic dendrite diameters of 25 and 100 μm.

The thermophysical properties used in the study are shown in Table 2, with solid densities, thermal conductivities, and thermal expansion coefficients for Al–4.5 wt% Cu and Al–6.0 wt% Mg alloys obtained directly [8] and the remaining properties evaluated as a weighted average of Al, Cu, and Mg values [8]. The average solid viscosity, $\bar{\mu}_s$, representing the contribution of free-floating dendrites to the mixture viscosity in the slurry region [1], was obtained by evaluating the integrated average of the solid viscosity expression, recommended by Ni and Incropera [6], across 70% of the slurry region (Table 2). As demonstrated by a scaling analysis of momentum transport in the slurry region [1], the average solid viscosity used to account for dendrite interactions in the slurry has a negligible impact on the transport of free-floating dendrites from the surface of the billet to the bottom of the sump.

To model interdendritic fluid flow in the rigid, mushy zone, the mushy zone permeability, K, is assumed to be isotropic and evaluated using the Blake–Kozeny expression, $K = \kappa_0(1 - g_s)^3/g_s^2$. Evaluation of the permeability coefficient, κ_0, for an equiaxed mushy zone relies on empirical data for flow through granular materials [9]. In this study, a permeability coefficient of $\kappa_0 = 6.67 \times 10^{-11}$ m^2, based on an assumed dendrite diameter of 100 μm, is used.

The model is closed by assuming thermodynamic equilibrium on the scale of individual control volumes and using the Al–Cu and Al–Mg phase diagrams, with constant equilibrium partition coefficients (Table 2) and thermodynamic relations developed by Bennon and Incropera [10] to account for both primary and eutectic solidification.

Table 2
Thermophysical properties and phase diagram parameters

Properties and phase diagram parameters	A1–4.5 wt% Cu	A1–6.0 wt% Mg
Liquid density, ρ_l (kg/m^3)	2460	2315
Solid density, ρ_s (kg/m^3)	2750	2650
Liquid specific heat, c_l (J/kg K)	1054	1097
Solid specific heat, c_s (J/kg K)	958	992
Latent heat of fusion, h_f (kJ/kg)	390	396
Liquid thermal conductivity, k_l (W/m K)	95.0	92.6
Solid thermal conductivity, k_s (W/m K)	180	130
Liquid diffusion coefficient, D_l^B (m^2/s)	5.0×10^{-9}	1.5×10^{-9}
Liquid viscosity, μ_l (kg/m s)	0.0013	0.0013
Average solid viscosity, $\bar{\mu}_s$ (kg/m s) $\bar{\mu}_s = \frac{1}{0.7g_{s,p}} \int_0^{0.7g_{s,p}} \mu_s \, dg_s$	$4.53\mu_l$ ($g_{s,p} = 0.15$); $4.96\mu_l$ ($g_{s,p} = 0.30$)	
Liquid thermal expansion coefficient, $\beta_{T,l}$ (K^{-1})	1.17×10^{-4}	1.22×10^{-4}
Solid thermal expansion coefficient, $\beta_{T,s}$ (K^{-1})	2.25×10^{-5}	2.3×10^{-5}
Liquid solutal expansion coefficient, $\beta_{S,l}$	−0.73	0.49
Solid solutal expansion coefficient, $\beta_{S,s}$	−0.87	0.59
Melting point of A1, T_{melt} (K)	933.5	933.5
Eutectic temperature, T_{eut} (K)	821.2	723.0
Maximum solid solubility, f^A_{max}	0.0565	0.17
Eutectic composition, f^A_{eut}	0.33	0.36
Equilibrium partition coefficient, k_p	0.171	0.472

2.2. Computational domain and boundary conditions

For 40 cm diameter billets, the length, L (Fig. 1), of the computational domain is set at 800 mm for Al–4.5 wt% Cu and 900 mm for Al–6.0 wt% Mg billets to insure that implementation of an adiabatic boundary condition is acceptable at $z = L$, for the fully solidified alloy ($\partial T/\partial z|_{z=L} = 0$). Additionally, the computational domains are discretized into 134×250 (Al–4.5 wt% Cu) and 134×290 (Al–6.0 wt% Mg) grids with control volume cross-sections of 1.5×1.5 mm in the liquid and two-phase regions ($g_s < 1$) of the domains. In the solid region, axial grid spacing was increased to take advantage of decreasing axial temperature gradients.

In each of the simulations, a *level pour* feeding system is modeled, with liquid metal at the nominal alloy composition uniformly introduced to the top of a water-cooled mold ($f^A|_{z=0} = f_0^A$, $v|_{z=0} = 0$). An inlet metal superheat of $\Delta T_{SH} = 32$ K ($T|_{z=0} = T_{liq} + \Delta T_{SH}$) and a casting velocity of $u_{cast} = 1.0$ mm/s are prescribed ($u|_{z=L} = u_{cast}$, $v|_{z=L} = 0$). To maintain mass continuity in the presence of shrinkage, the metal inlet velocity is set to $u|_{z=0} = (\rho_s/\rho_l)u_{cast}$ under steady-state conditions. At the billet surface, a *no slip* boundary condition ($u|_{r=R} = 0$) is applied in the liquid and slurry regions ($g_s < g_{s,p}$), and an axially translating boundary ($u|_{r=R} = u_{cast}$) is applied in the rigid, mushy zone and solid regions ($g_s \geq g_{s,p}$), with the assumption that no liquid escapes the computational domain ($v|_{r=R} = 0$). The energy boundary condition at the billet surface is applied through a variable heat transfer coefficient, $U = q''/(T|_{r=R} - T_c)$.

The simulated casting assembly consists of a 120 mm adiabatic section ($0 \leq z < 120$ mm) followed by a 60 mm mold section. In the mold section, Katgerman et al. [11] suggested that the formation of an 'air gap' between the billet surface and mold could be approximated by weighting two distinct heat transfer coefficients according to the solid and liquid volume fractions. One coefficient corresponds to the heat extracted through direct mold contact, and the other coefficient corresponds to conduction and radiation across the air gap. This approach is used in the current study such that

$$U = g_s|_{r=R} \cdot U_{gap} + g_l|_{r=R} \cdot U_{mold} \quad (120 \leq z < 180 \text{ mm}) \tag{1}$$

where U_{mold} and U_{gap} are coefficients representing heat removed through direct mold contact and cooling across the air gap, respectively. Based on heat transfer coefficients obtained in experimental studies [11–13], mold and air gap coefficients of $U_{mold} = 1500$ W/m^2 K and $U_{gap} = 150$ W/m^2 K are used with $T_c = 300$ K for the convection sink (cooling water) temperature.

Heat transfer coefficient distributions in the secondary cooling region (Fig. 1) are also based on measurements made with DC cast billets [12,14], where heat transfer coefficients were observed to exhibit sharp, nearly linear increases in the impinging jet region, and

achieved a maximum within an axial length of 5 to 10 mm. The subsequent decreases occurred over axial lengths of approximately 30 to 60 mm, with nearly uniform values maintained along the remaining length of the billet. Accordingly, the heat transfer coefficient is presumed to increase linearly in the impinging jet region to some maximum value, U_{max}, and then decrease linearly to some uniform value, U_{film}, such that

$$U = U_{gap} + \frac{z - z_1}{z_2 - z_1}\left(U_{max} - U_{gap}\right) \quad (180 \le z < 190 \text{ mm}) \tag{2}$$

$$U = U_{max} + \frac{z - z_2}{z_3 - z_2}(U_{film} - U_{max}) \quad (190 \le z < 230 \text{ mm}) \tag{3}$$

$$U = U_{film} \quad (z \ge 230 \text{ mm}) \tag{4}$$

where $z_1 = 180$ mm, $z_2 = 190$ mm, and $z_3 = 230$ mm.

Estimates for U_{max} and U_{film} are obtained from various sources, including Tarapore [14] who reported a maximum heat transfer coefficient of approximately 22,000 W/m^2 K and a uniform, falling film coefficient of approximately 12,000 W/m^2 K for 40 cm diameter billets cast at 1.0 mm/s. Grun et al. [13] suggested that the heat transfer coefficient in the secondary cooling region generally varies between 7000 and 30,000 W/m^2 K for DC cast billets. In the current study, a maximum heat transfer coefficient of $U_{max} = 20{,}000$ W/m^2 K is used with $U_{film} = 10{,}000$ W/m^2 K.

2.3. Solution methodology

The numerical solution of the conservation equations (Table 1) is implemented through the use of a control volume formulation and the SIMPLER algorithm [15]. The procedures outlined by Bennon and Incropera [10] are used with upwind differencing to discretize all source terms with the exception of the so-called *advection-like source terms* in the species equation. For these terms, the discretization procedure was modified to insure that solid and liquid advection is properly calculated when both phases simultaneously cross control volume interfaces [16].

Once discretized, the system of conservation equations is solved by a *tridiagonal matrix algorithm* (TDMA), line-by-line solver with a block correction method. For convergence to be established at a given time step, the normalized residuals of the energy and species equations must be less than 10^{-4}, the sum of all *fictitious mass sources* in the pressure equation [15] must be less than 10^{-8} kg/s, and the largest absolute value of the fictitious mass sources divided by the maximum flow rate across a control volume interface in the computational domain must be less than 10^{-3}. Additionally, the criteria must be satisfied for five consecutive iterations before convergence is declared at a given time step. To decrease the total computational time, a steady state solution was first obtained by solving the energy equation exclusively, with the resulting solid fraction and temperature distribution used as initial conditions.

While a steady state solution was obtained for an Al–4.5 wt% Cu billet without free-floating dendrites ($g_{s,p} = 0$), attempts to obtain steady state numerical solutions with free-floating dendrites ($g_{s,p} > 0$) were unsuccessful. Recognizing that converged solutions could not be obtained without the time-dependent terms in Table 1, transient simulations were marched forward in time with convergence rigorously enforced at each time step. As the simulations proceeded forward in time, a quasi-steady state was reached where transient variations in the dependent variables reached a minimum range. However, once the quasi-steady state was reached, time steps from 0.3 to 0.75 s were still required to maintain convergence.

Marching the solutions forward in time revealed that slight transient flow field variations persisted near the billet centerline due to interactions between the highly coupled transport equations and the discontinuous interface ($g_s = g_{s,p}$) that separates the slurry region from the rigid dendritic structure [1]. At this interface, the permeability, K, has a dominant effect on momentum transport, and therefore the local flow field, in the mushy region [17]. While the local flow field depends strongly on the permeability, and therefore the location of the rigid, mushy zone interface, the location of this interface depends on the local solid fraction, which, in turn, depends on the local solute composition and, hence, the local flow field. Though not as significant near the billet surface, where temperature gradients are high and the position of the rigid, mushy zone interface ($g_s = g_{s,p}$) is well established, near the centerline of the billets ($r < 50$ mm), this highly non-linear relationship results in a slight transient variation in the position of the rigid, mushy zone interface over a range of 1 to 2 control volumes (~1.5–3 mm). The oscillatory shifting of this interface near the center of the billets with time, which persists as converged, transient solutions are marched forward, has little impact on variations of dependent variables throughout the rest of the billet.

With negligible, transient variations of dependent variables through most of the billet, the only concern regarding the time-dependent shifting of the rigid, mushy zone interface ($g_s = g_{s,p}$) near the centerline ($r < 50$ mm) is its impact on the predicted surface-to-centerline solute distribution in the solid billet. To

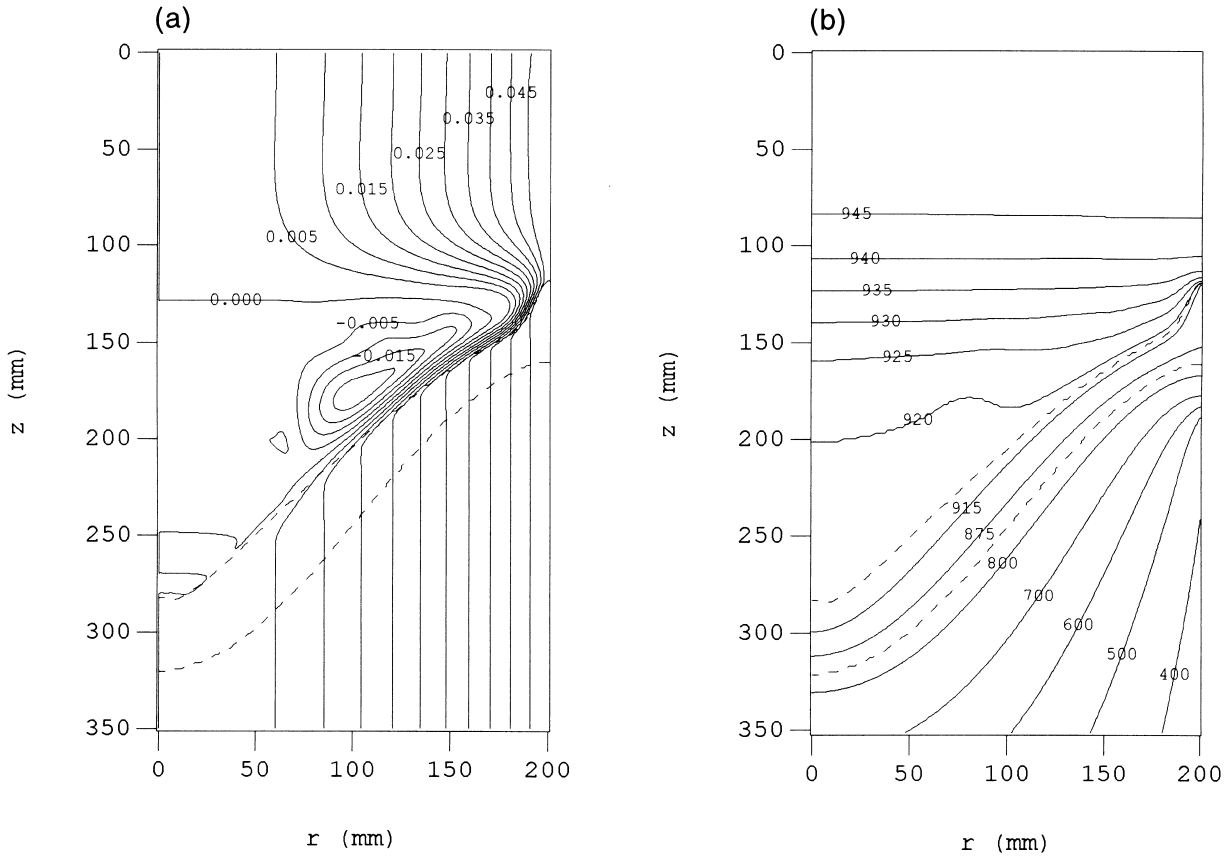

Fig. 2. Case 1 ($g_{s,p} = 0$): (a) mixture streamlines and (b) temperature contours in Kelvins.

determine the variation of the local solute composition with time, values at each radial location of a transverse section in the solid region were recorded every 3 s over a 600 s time interval, once the simulation had reached its quasi-steady state. The solute composition at each radial location was then averaged over the 600 s interval, and the standard deviation was evaluated. Standard deviations of less than 1.0% were recorded away from the centerline ($r \geq 50$ mm) and less than 3.0% near the centerline ($r < 50$ mm), suggesting that time-dependent variations have a negligible effect on the results of the quasi-steady, converged solutions as they proceed. Hence, the surface-to-centerline solute distributions presented in the following sections were obtained by averaging the solute composition at each radial location over the 600 s interval.

3. Results

3.1. Al–4.5 wt% Cu alloy

3.1.1. Case 1: no free-floating dendrites ($g_{s,p} = 0$)

If solidification of Al-4.5 wt% Cu is modeled without the development of a slurry of free-floating dendrites, the solid forms only as a rigid structure, which moves uniformly at the casting speed, and macrosegregation is dominated by the flow of copper-rich interdendritic liquid. Mixture streamlines ($\partial\psi = -\rho v r \partial r = \rho u r \partial r$) and isotherms are shown in Fig. 2, with the liquidus ($g_s = 0$) and solidus ($g_s = 1$) interfaces superimposed as dashed curves. Liquid metal enters the top of the computational domain at a uniform velocity and temperature, and proceeds in the axial direction before accelerating and flowing preferentially toward the surface of the billet where thermal and solutal buoyancy forces maintain a descending flow of cooler, solutally heavier (copper-rich) liquid, along the liquidus interface (Fig. 2a). This flow, characterized by velocities as large as 10 mm/s, is ultimately deflected upward, creating a strong clockwise recirculation (Fig. 2a). The largest ascending velocities in the recirculation cell are approximately 5 mm/s, while the remaining fluid in the recirculation region ($r < 70$ mm) ascends slowly toward the incoming flow at velocities in the order of the casting speed ($\sim$1 mm/s). Within the mushy zone ($0 < g_s < 1$), significant buoyancy driven flow occurs up to a solid

volume fraction of 10% (Fig. 2a), above which interdendritic liquid velocities (relative to the solid phase) decrease appreciably to values much less than 0.1 mm/s. The recirculation in the melt yields a relatively uniform temperature distribution in the sump (Fig. 2b), above which temperatures decrease slightly in the casting direction, as heat is conducted toward the cooler, underlying liquid. Near the surface of the billet and in the solid region, temperature gradients are orders of magnitude larger than those in the melt due to the high rate of heat extraction at the surface.

The liquid flow in Case 1 (Fig. 2a) sweeps copper-rich interdendritic liquid toward the centerline, creating a copper-rich core of positive centerline segregation (Figs. 3 and 4). In addition to the positively segregated core, there is a thin layer of *subsurface enrichment* (positive segregation) and an adjoining *depleted region* of negative segregation. Both regions are commonly observed in commercially cast ingots [2–4] and were also predicted by Reddy and Beckermann [18].

The thin layer of positive segregation at the billet surface is due to a shrinkage induced flow of copper-rich interdendritic liquid resulting from high solidification rates. In contrast, the radial extent of negative segregation in the depleted region (Fig. 4) coincides with the radial extent of the constricted flow, as it rapidly accelerates toward the billet surface, before being deflected and descending along the liquidus interface (Fig. 2a). As this flow impinges on the rigid dendritic structure, it floods the mushy zone with liquid at the nominal copper composition (Fig. 3), thereby replacing the copper-rich liquid which descends along the liquidus interface. This impinging flow, therefore, sustains solidification and development of the copper-depleted region commonly observed near the surface of DC cast ingots [2–4].

With decreasing radius from the depleted region (Fig. 4), the final copper composition is characterized by locally sharp variations, which are followed by positive centerline segregation due to the flow of copper-rich liquid to the bottom of the sump (Figs. 2a and 3). The sharp variations in copper composition ($125 < r < 185$ mm) are attributed to the existence of large solid fraction gradients and the inability to adequately resolve the flow field just above and below the liquidus interface.

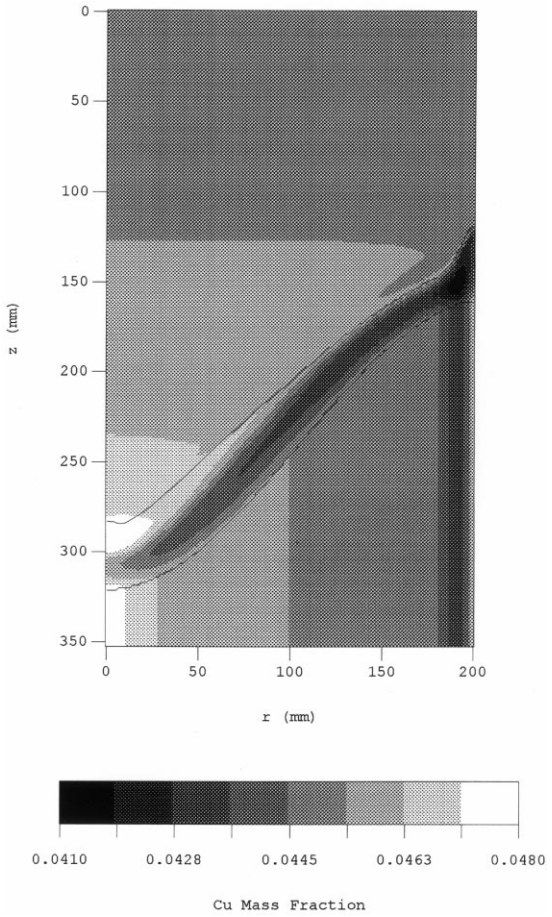

Fig. 3. Mixture copper composition field for Case 1 ($g_{s,p} = 0$).

3.2. Macrosegregation with free-floating dendrites

3.2.1. Effect of the packing fraction: Cases 2 and 3

Packing fractions of 15 and 30% are used in Cases 2 and 3, respectively, with a characteristic dendrite diameter of 25 μm to model the slurry of free-floating dendrites that develops during DC casting of Al–4.5 wt% Cu billets. Macrosegregation now depends on the transport of copper-depleted, free-floating dendrites, as well as copper-rich liquid. Solid fraction contours, mixture streamlines, and temperature contours for Cases 2 and 3 are shown in Figs. 5–7, respectively, 600 s after the simulations have reached their quasi-steady state. Additionally, in Figs. 6 and 7, the liquidus ($g_s = 0$) and solidus ($g_s = 1$) interfaces, as well as the interface between the slurry region and rigid dendritic structure ($g_s = g_{s,p}$) are superimposed as dashed curves.

In both Cases 2 and 3, general characteristics of the flow field (Fig. 6) are similar to those in Case 1 (Fig. 2a), with the incoming flow rapidly accelerating toward the billet surface and subsequently descending along the interface of the rigid, mushy zone. However, in Cases 2 and 3, free-floating dendrites are swept along this interface and ultimately join with the rigid dendritic structure or recirculate back into the slurry region (Fig. 6). Also, acceleration of the incoming flow is more severe in these cases due to the presence of free-floating dendrites in the liquid, which increase the buoyancy force imposed on the mixture [1]. As the packing fraction increases, the solid fraction in the

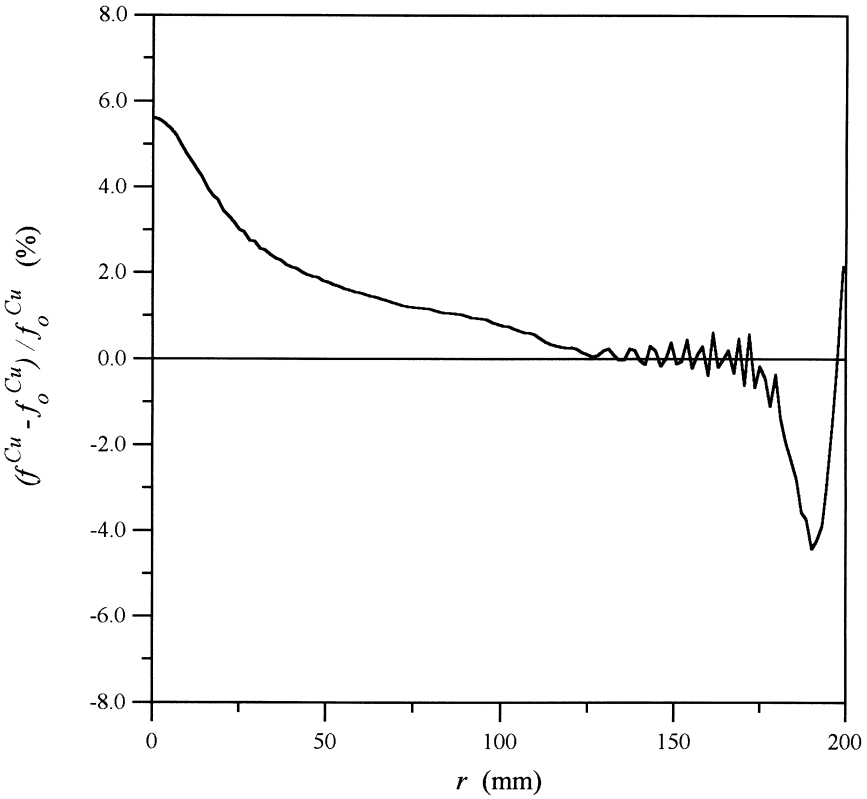

Fig. 4. Radial distribution of the copper composition in the final casting for Case 1 ($g_{s,p} = 0$).

slurry region increases, thereby increasing buoyancy forces such that, velocities as high as 17 mm/s in Case 2 and 30 mm/s in Case 3 are predicted.

The mixture composition fields for Cases 2 and 3 appear in Fig. 8 with the liquidus and solidus interfaces, as well as the interface between the slurry region and rigid, mushy zone, superimposed as solid curves. In both cases, solutal stratification is observed in the slurry, near the center of the billet, as copper-depleted dendrites settle along the horizontal interface of the rigid, mushy zone. Just below this interface, in the regions bounded by $0.15 \leq g_s \leq 0.17$ in Fig. 5a and $0.30 \leq g_s \leq 0.32$ in Fig. 5b, distributions of the solid fraction, temperature (Fig. 7), and copper composition (Fig. 8) are nearly uniform. These regions develop as copper-depleted dendrites settle to the bottom of the sump, which becomes increasingly copper-depleted, with an attendant increase in the local solidus and liquidus temperatures. As free-floating dendrites continue to accumulate, the increasing solidus and liquidus temperatures enhance solidification, causing the interface of the rigid dendritic structure to ascend toward the inlet. Ultimately, as the transient simulations reach their quasi-steady solution, a point of equilibrium is reached where the continuous accumulation of copper-depleted dendrites settling into the rigid dendritic structure is balanced by downward advection of the packed dendrites such that, the rigid, mushy zone interface at $g_s = g_{s,p}$ no longer ascends toward the inlet. As the packed, copper-depleted dendrites and accompanying interdendritic liquid near the center of the billets are advected away from this interface, a significant amount of phase change does not occur until heat extraction at the billet surface begins to significantly reduce the local temperature (Fig. 7). Hence, the packed bed of dendrites (Fig. 5) retains a solid fraction close to the packing fraction at which the free-floating dendrites settle, until it is advected into the region of accelerated cooling, where solidification intensifies and proceeds to completion.

Due to the accumulation of free-floating dendrites at the bottom of the sump, the rigid, mushy zone ($g_{s,p} \leq g_s < 1$) in Cases 2 and 3 may be subdivided into two fundamentally different sub-regions (Fig. 9). These regions include a uniformly packed bed of solute-depleted dendrites with a relatively uniform solid fraction, temperature, and composition, and the remaining rigid dendritic structure ($0.17 < g_s < 1.0$ in Fig. 5a; $0.32 < g_s < 1.0$ in Fig. 5b) across which significant solid fraction and temperature gradients exist as solidi-

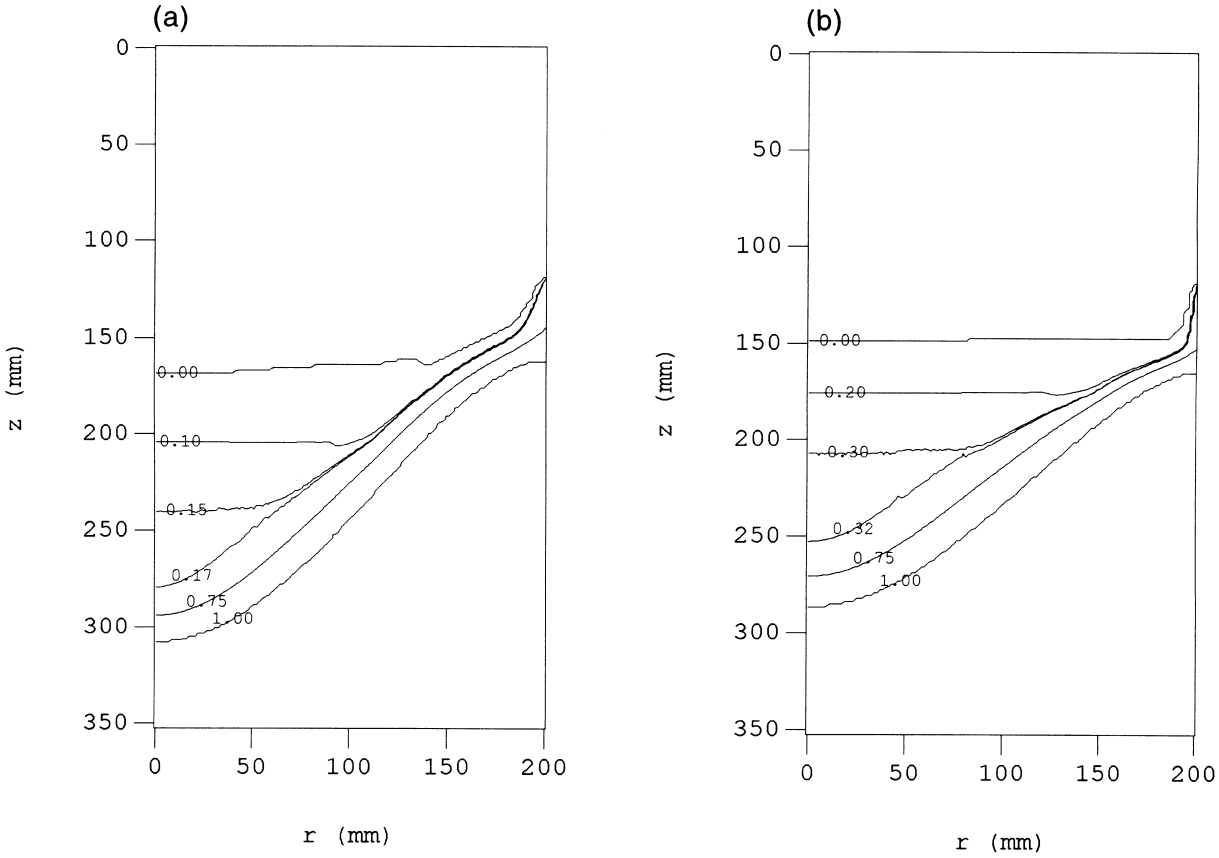

Fig. 5. Solid volume fraction contours for (a) Case 2 ($g_{s,p} = 0.15$) and (b) Case 3 ($g_{s,p} = 0.30$).

fication proceeds to completion. Therefore, the horizontal part of the rigid, mushy zone interfaces ($g_s = g_{s,p}$) in Fig. 5 shows the extent to which the sump has been 'filled' with the settled free-floating dendrites under quasi-steady conditions (Fig. 9).

Having verified that the model predicts the settling of solute-depleted dendrites to the bottom of the sump, as suggested experimentally [2–4], the effect of settling on the final copper distribution is shown in Fig. 10. For both packing fractions, the accumulation of copper-depleted dendrites at the bottom of the sump yields the negative centerline segregation observed in DC cast ingots [2–4,19]. Furthermore, the radial extent of the negatively segregated regions correlates well with the radial extent of the uniformly packed beds of copper-depleted dendrites at the bottom of the sumps (Fig. 5). These results strongly suggest that the radial extent and degree to which negative segregation occurs near the centerline of DC cast ingots, are directly related to the radial extent and level to which copper-depleted dendrites accumulate at the bottom of the sump. Comparing Cases 2 and 3, the degree of negative segregation is seen to increase with increasing packing fraction (Fig. 10) due to the settling of a larger volume of solute-depleted solid.

Fig. 10 also shows *enriched regions* of positive segregation, also observed in DC cast ingots [2–4], adjacent to the negatively segregated core. Fig. 8 shows that copper-depleted solid settling near the center of the billet displaces copper-rich liquid upward, while Fig. 6 indicates that the clockwise recirculating flow returns this liquid toward the surface of the billet. The copper-rich liquid ultimately turns again when it encounters the inlet flow and descends into the interface of the rigid, mushy zone before reaching the billet surface (Fig. 6), thus flooding the rigid dendritic structure with solute-rich liquid and creating the enriched regions of Fig. 10. These regions of positive segregation are, therefore, a direct consequence of solutal stratification occurring in the slurry due to settling of solute-depleted solid at the expense of solute-rich liquid.

As in Case 1, the distributions in Fig. 10 exhibit local regions with sharp variations in composition, which are due to inadequate resolution of locally one-dimensional flows which must traverse the interface of a rigid, mushy zone represented by a series of rec-

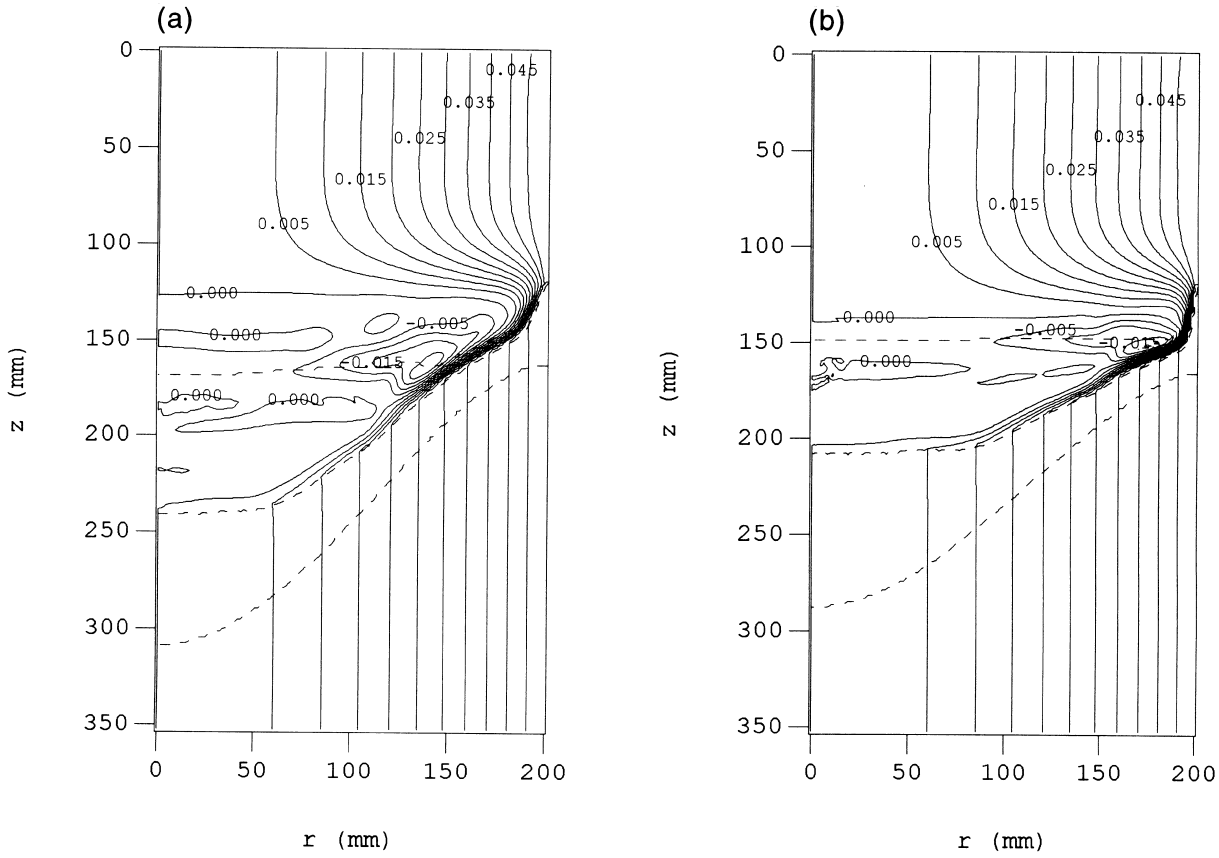

Fig. 6. Mixture streamlines for (a) Case 2 ($g_{s,p} = 0.15$) and (b) Case 3 ($g_{s,p} = 0.30$).

tangular control volumes. The increased severity of the variations in Case 2 (Fig. 10a) relative to Case 1 (Fig. 4) is due to increased velocities near the interface of the mushy zone and the low permeability of the rigid dendritic structure. Ultimately, as velocities in the slurry decrease toward the centerline and the mushy zone interface becomes more horizontal (Fig. 6a), the variations decay to near zero (Fig. 10a). The local variations in composition are less severe for Case 3 (Fig. 10b) due to the more horizontal mushy zone interface at $150 < r < 185$ mm (Fig. 5b).

Fig. 10(a) and (b) also show depleted regions of negative segregation near the surface of the billets. The thickness of this region is smaller for Case 3 due to the increased acceleration and constriction of the incoming flow near the billet surface (Fig. 6b). This strong correlation between constriction of the incoming, nominal composition flow and the thickness of the depleted region in Cases 1–3 confirms that development of this region in DC cast ingots is controlled by the flow of incoming liquid, as it accelerates towards the billet surface and impinges on the rigid, mushy zone (Figs. 2a, 6a, and 6b).

Finally, the degree of segregation at the billet surface (Fig. 10) decreases with decreasing thickness of the rigid dendritic structure in Cases 2 and 3 (Fig. 5). This result is due to the increased packing fraction, which allows more of the solid phase to be advected from the surface of the billet. This reduction in shrinkage induced segregation at the surface of billets due to the transport of free-floating dendrites was also observed by Reddy and Beckermann [20].

3.2.2. *Effect of the characteristic dendrite diameter: Case 4*

In Case 4, the characteristic dendrite diameter is 100 μm with a packing fraction of 30%, and results may be compared with those of Case 3, for which $d = 25$ μm and $g_{s,p} = 0.3$ (Fig. 11). In Case 4 ($d = 100$ μm), the difference between axial velocities of the free-floating dendrites and the surrounding liquid is approximately an order of magnitude larger than Case 3 ($d = 25$ μm). As a result, an increase in the rate at which copper-depleted solid accumulates at the bottom of the sump is observed and accompanied by an increase in the rate at which the surrounding copper-

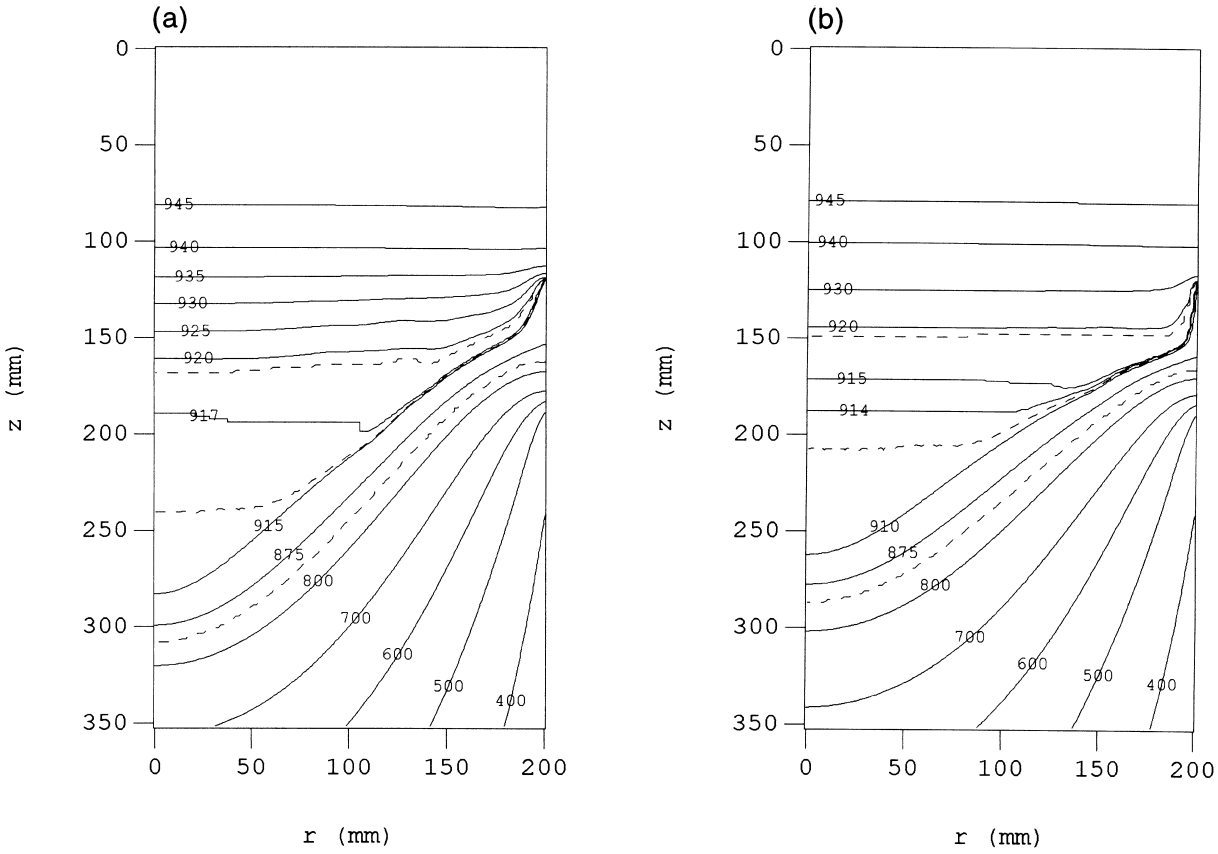

Fig. 7. Temperature contours in Kelvins for (a) Case 2 ($g_{s,p} = 0.15$) and (b) Case 3 ($g_{s,p} = 0.30$).

rich liquid is displaced upwards. Hence, with increasing d, liquid in the upper part of the slurry region, which is recirculated toward the billet surface, becomes increasingly copper-rich, while solid accumulating at the bottom of the sump becomes increasingly copper-depleted. As shown in Fig. 11, the net effect is larger degrees of negative and positive segregation at the centerline and in the enriched region, respectively.

3.3. Al–6.0 wt% Mg alloy

In contrast to an Al–4.5 wt% Cu alloy, solidification of an Al–6.0 wt% Mg alloy involves the rejection of the lighter of the two constituents (magnesium). In Cases 5 and 6, packing fractions are 15 and 30%, respectively, with a characteristic dendrite diameter of 25 μm. Mixture streamlines and magnesium distributions are shown in Figs. 12 and 13, respectively, 1100 s after the simulations have reached a quasi-steady state. Again, the liquidus and solidus interfaces and the interface between the slurry region and the rigid, mushy zone are superimposed as the dashed curves in Fig. 12 and solid curves in Fig. 13.

As in the Al–4.5 wt% Cu billets, free-floating dendrites are swept towards the centerline as the incoming liquid accelerates towards the billet surface and down the interface of the rigid, mushy zone with velocities as high as 23 mm/s in Case 5 and 44 mm/s in Case 6 (Fig. 12a and b). Solute-depleted dendrites settle once again into the sump at the expense of solute-rich liquid which is displaced upward (Fig. 13). Hence, as in the Al–4.5 wt% Cu cases, the slurry region becomes solutally stratified with free-floating solute-depleted solid accumulating at the bottom of the sump, forming a region of uniformly packed dendrites whose extent increases with increasing packing fraction (Fig. 13). This equivalent behavior in both Al–4.5 wt% Cu and Al–6.0 wt% Mg alloys results from the strong dependence of the buoyancy force in the slurry region, on the local solid fraction and the comparatively weak effect of solutal gradients [1].

While solutal gradients do not appreciably affect momentum transfer nor segregation phenomena in the slurry region, there is a significant effect on flow in the melt above the slurry where $g_s = 0$ (Fig. 12). In both Cases 5 and 6, a plume of magnesium-rich liquid ascends along the centerline and deflects the solutally heavier incoming flow at the top of the computational

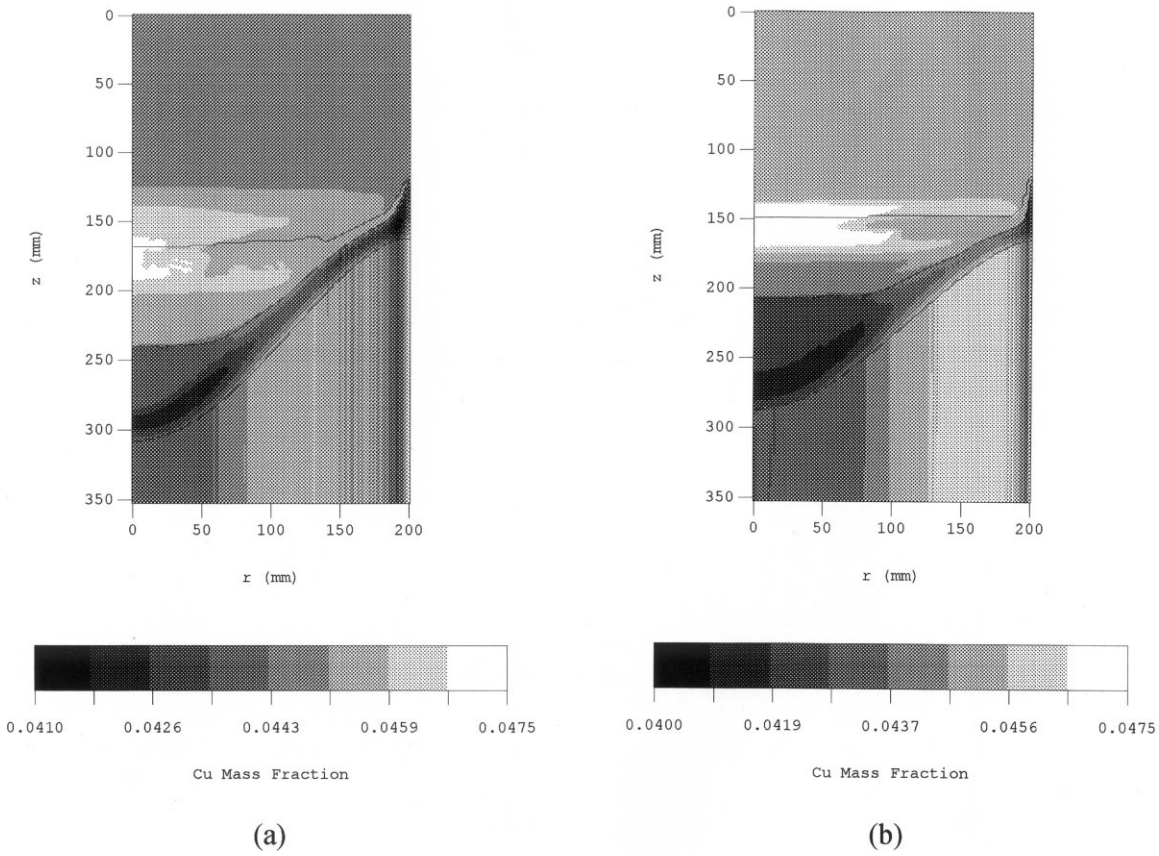

Fig. 8. Mixture copper composition field for (a) Case 2 ($g_{s,p} = 0.15$) and (b) Case 3 ($g_{s,p} = 0.30$).

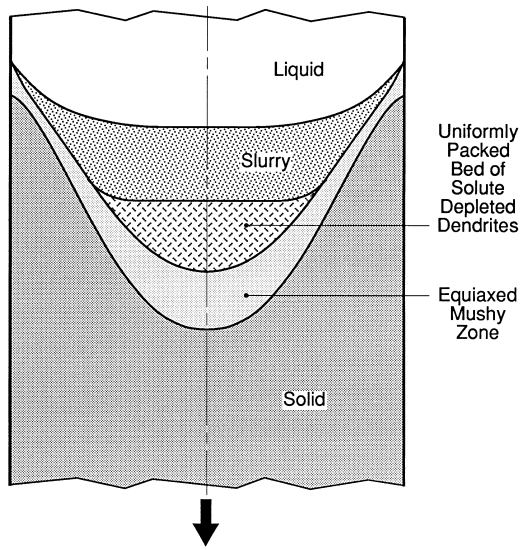

Fig. 9. Distinct two-phase regions associated with DC cast billets.

domain (Figs. 12 and 13). These plumes form as magnesium-rich liquid is displaced upward through the slurry region and into the melt, leading to an accumulation of magnesium-rich liquid just above the liquidus interface (Fig. 13). While a similar accumulation of copper-rich liquid occurs in the Al–4.5 wt% Cu billets (Fig. 8), the copper-rich liquid is heavier than liquid at the mold inlet and, consequently, does not ascend to the top of the computational domain.

Clearly, from Fig. 12, the specification of uniform inlet conditions for the computational domain is a poor assumption for the Al–6.0 wt% Mg simulations, since, in reality, the upflow of magnesium-rich liquid should continue unimpeded, thus interacting with the incoming flow and potentially introducing turbulence at the inlet. The best method for modeling DC casting of Al–6.0 wt% Mg would be to extend the computational domain upward, and to include liquid flow in the distribution pan and/or the trough above the mold assembly.

The final radial distributions of magnesium for Cases 5 and 6 are shown in Fig. 14. Trends are ident-

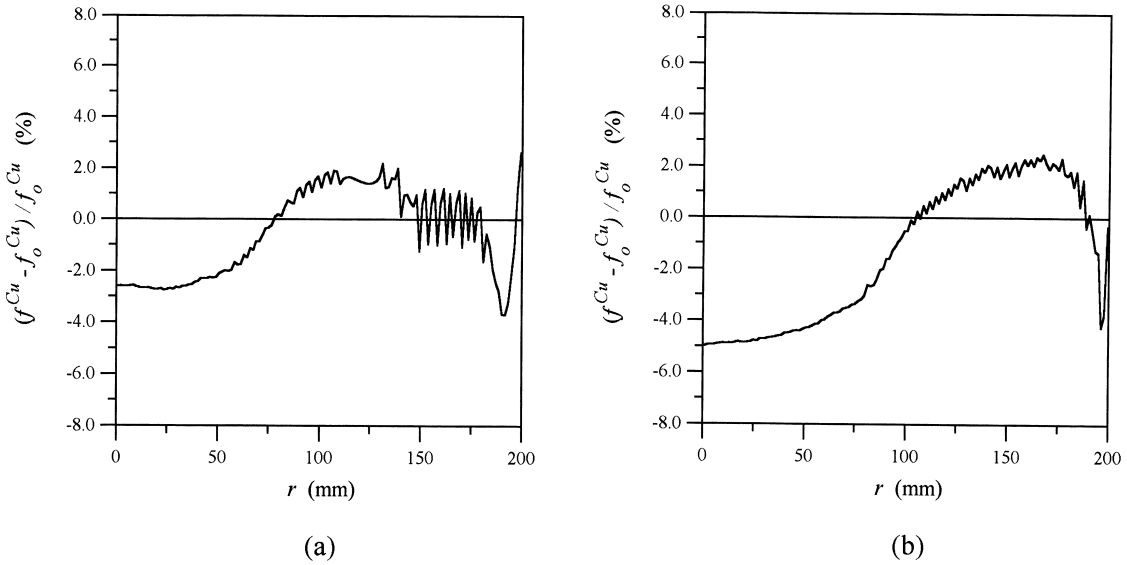

Fig. 10. Radial distribution of the copper composition in the final casting for (a) Case 2 ($g_{s,p} = 0.15$) and (b) Case 3 ($g_{s,p} = 0.30$).

ical to those of the Al–4.5 wt% Cu billets, including the development of negatively segregated depleted regions adjacent to positively segregated enriched regions near the billet surface and negative segregation at the centerline. Additionally, as in the Al–4.5 wt% Cu cases, the degree of negative segregation at the cen-

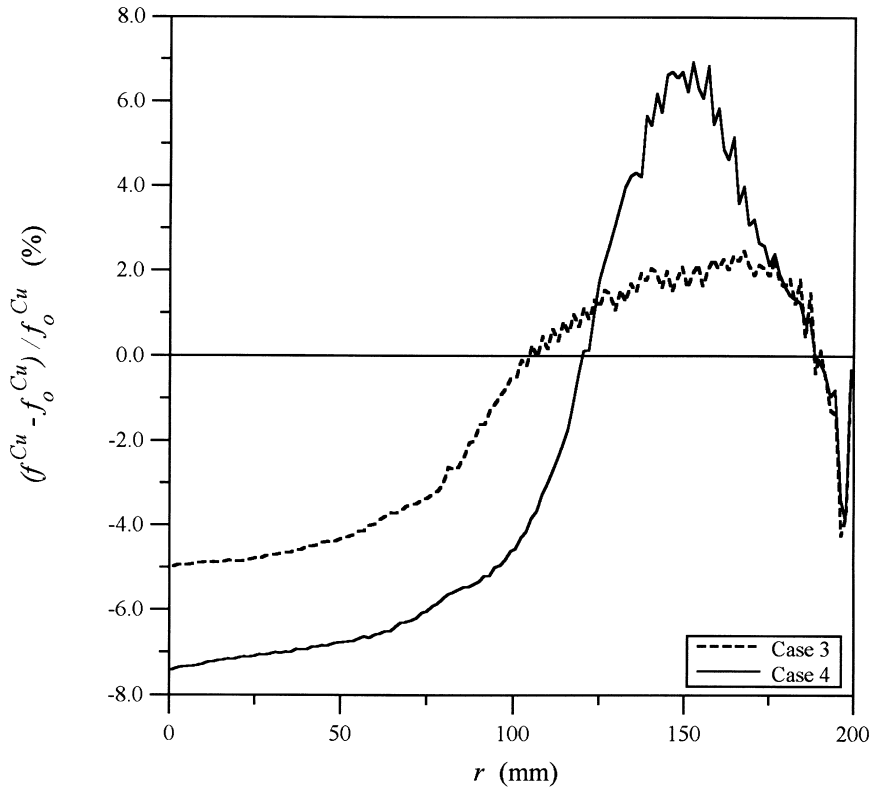

Fig. 11. Radial distribution of the copper composition in the final casting for Case 3 ($d = 25$ μm) and Case 4 ($d = 100$ μm).

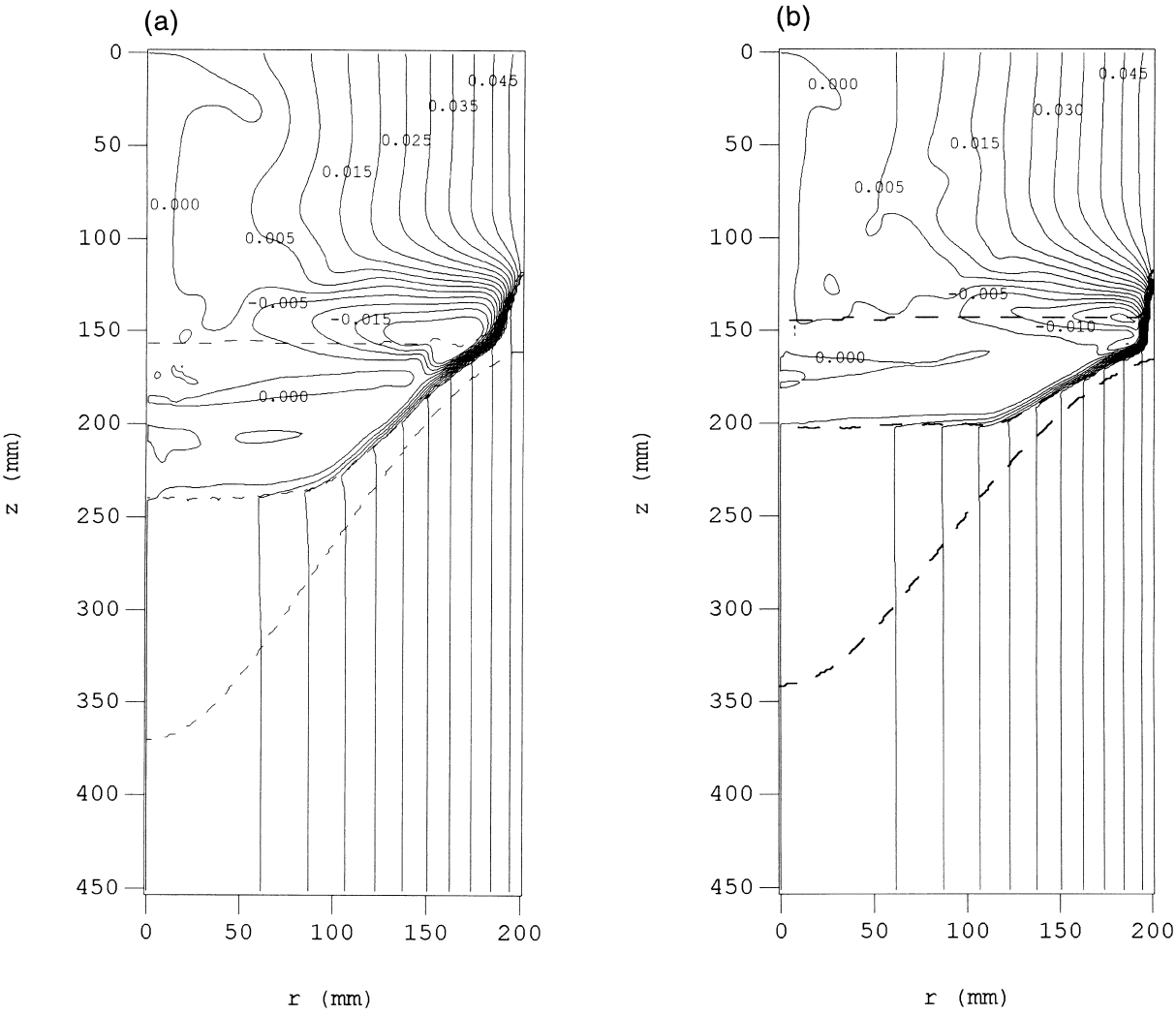

Fig. 12. Mixture streamlines for (a) Case 5 ($g_{s,p} = 0.15$) and (b) Case 6 ($g_{s,p} = 0.30$).

ter of the billet increases with increasing $g_{s,p}$ due to the increased volume of solid settling at the bottom of the sump and a radially thinner depleted region is observed near the surface due to the enhanced acceleration and constriction of the incoming flow (Fig. 12). The basic trend in Fig. 14 is consistent with experimental studies that have observed similar segregation phenomena in DC cast ingots for both copper and magnesium alloys [2–4].

For Case 7, the dendrite diameter and packing fraction are fixed at 100 μm and 30%, respectively. Once again, the increase in the characteristic dendrite diameter leads to the coupled effect of a higher degree of negative segregation near the center of the billet and increased positive segregation near the billet surface (Fig. 15).

4. Conclusions

DC casting simulations were conducted using the mixture model proposed by Vreeman et al. [1] to predict macrosegregation in Al–4.5 wt% Cu and Al–6.0 wt% Mg billets. The mixture model accounts for macrosegregation due to fluid flow in the melt and mushy zone, as well as the transport of solute-depleted, free-floating dendrites. Since neither the packing fraction at which free-floating dendrites coalesce to form a rigid dendritic structure nor the dendrite size distribution in the slurry regions of DC cast ingots are explicitly known, a parametric study was conducted in which order-of-magnitude estimates of the packing fraction, $g_{s,p}$, and characteristic dendrite diameter, d, were made to evaluate their effect on the macrosegre-

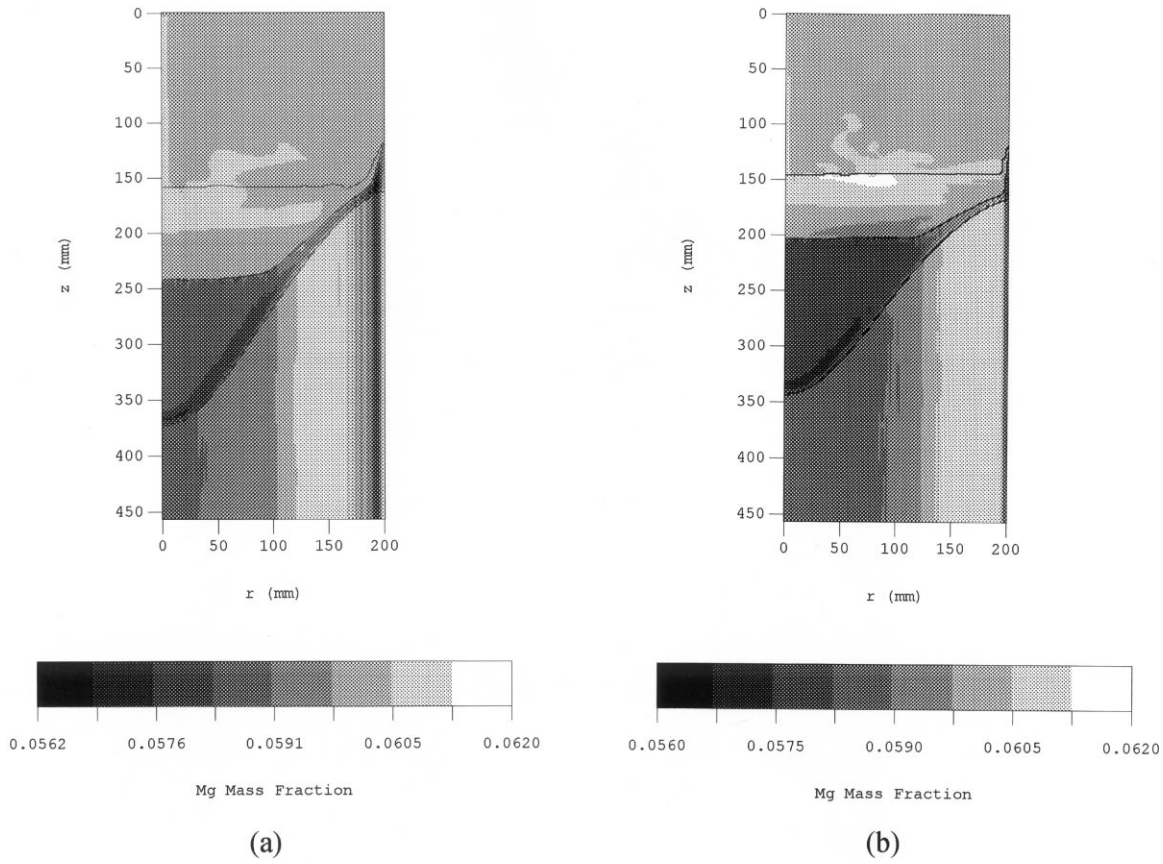

Fig. 13. Mixture magnesium composition field for (a) Case 5 ($g_{s,p} = 0.15$) and (b) Case 6 ($g_{s,p} = 0.30$).

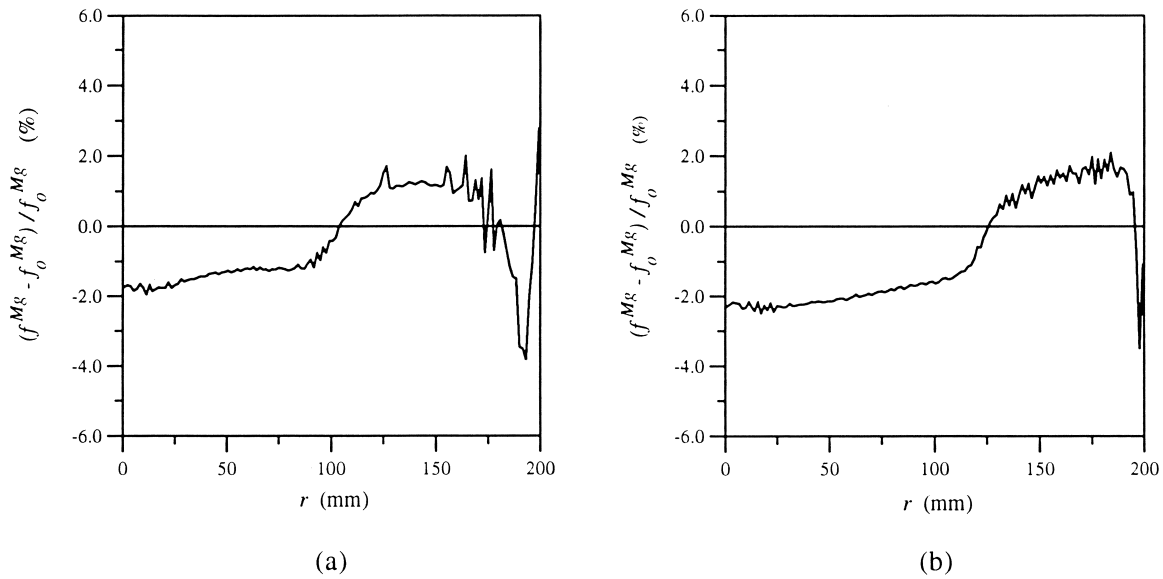

Fig. 14. Radial distribution of the magnesium composition in the final casting for (a) Case 5 ($g_{s,p} = 0.15$) and (b) Case 6 ($g_{s,p} = 0.30$).

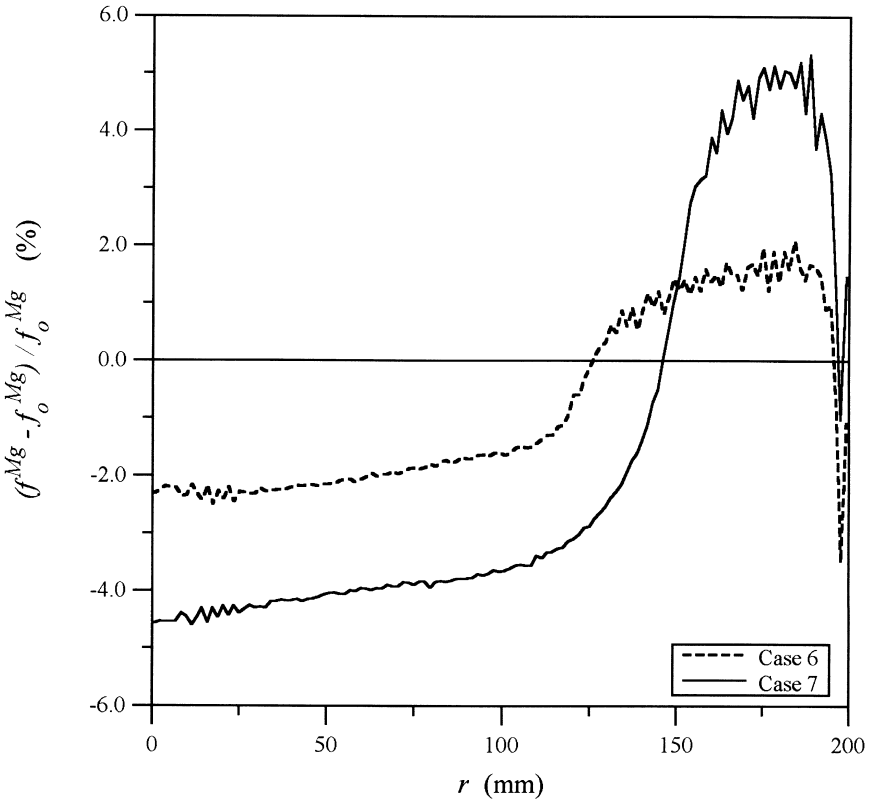

Fig. 15. Radial distribution of the magnesium composition in the final casting for Case 6 ($d = 25$ μm) and Case 7 ($d = 100$ μm).

gation predicted in 40 cm diameter billets produced under otherwise identical casting conditions.

In simulations of both Al–4.5 wt% Cu and Al–6.0 wt% Mg billets for which the transport of free-floating dendrites was modeled, the predicted surface-to-centerline macrosegregation exhibited trends observed in DC cast ingots [2–4,19]. These trends include the presence of negative segregation at the centerline, an enriched region of positive segregation away from the centerline, an adjacent depleted region, and a thin layer of inverse segregation at the billet surface. In addition to predicting these commonly observed macrosegregation trends, the simulations identified their physical origins.

Negative segregation at the center of the billets develops as solute-depleted dendrites are advected along the interface of the rigid, mushy zone and settle near the centerline to form a uniformly packed region at the bottom of the sump. As the free-floating dendrites settle near the centerline, the surrounding solute-rich liquid is displaced upward and experiences recirculation toward the surface of the billet and down into the interface of the rigid, mushy zone, establishing the region of positive segregation commonly observed in DC cast ingots [2–4].

The development of solute-depleted regions just within the billet surface is caused by acceleration and constriction of the incoming flow, which continuously floods the rigid, mushy zone with liquid at the nominal composition, thus insuring that solid developing in this region is solute-depleted. In contrast, the increase in solute composition at the billet surface is attributed to the flow of solute-rich interdendritic liquid in the rigid, mushy zone needed to feed the shrinkage associated with solidification rates at the surface.

The parametric study of the packing fraction, $g_{s,p}$, revealed that negative segregation at the centerline increases with increasing $g_{s,p}$ due to the increased volume of solute-depleted solid that accumulates at the bottom of the sump. Also, the thickness of the depleted region near the surface decreases with increasing $g_{s,p}$ due to increased constriction and acceleration of the incoming flow. Likewise, increasing the characteristic dendrite diameter, d, significantly increases negative segregation at the centerline, due to the increased settling rate of solute-depleted dendrites. Additionally, with higher dendrite settling rates, solute-rich liquid in the slurry is displaced upward and recirculated at higher rates, leading to greater positive segregation in the enriched region.

While commonly observed macrosegregation trends

were predicted and their physical origins clearly identified for Al–4.5 wt% Cu and Al–6.0 wt% Mg billets, the solidification model of this study is viewed as a first order model limited by its simplifying assumptions. Model improvements will be required before quantitatively accurate predictions of macrosegregation in DC cast ingots can be made. Specific improvements are apparent from the results of the study. For example, since the degree of negative segregation at the centerline depends on the specified packing fraction, further study is needed on the manner in which free-floating dendrites coalesce to form a rigid dendritic structure. Additionally, with levels of macrosegregation at the centerline and enriched regions strongly dependent on dendrite settling rates, realistic dendrite diameter variations in the slurry, dendrite morphology considerations for solid–liquid drag, and accurate solid–liquid density values in the slurry region are necessary before quantitatively accurate predictions can be made on a case by case basis.

Finally, despite the adherence to rigorous convergence criteria at every time step, the inability of the rectangular grid used in the study to smoothly resolve flow characteristics along portions of the rigid, mushy zone interface, where velocities are highest, suggests that the quantitative composition results exhibit a degree of grid dependence. However, the prediction of experimentally established macrosegregation trends [2–4,19] and careful scrutiny of the numerical results from the macro-scale of the computational domain down to individual control volumes, suggest that the results do capture the fundamental physical phenomena responsible for macrosegregation in DC cast billets, including the rejection of alloying elements, fluid flow due to buoyancy and shrinkage, and the settling of free-floating dendrites. Therefore, while compositions at individual control volumes will change with grid variations, the fundamental trends (specific regions of positive and negative segregation) will be preserved.

Despite these limitations, the manner in which each region of segregation develops in commercially cast ingots and the coupling between these regions have been clearly established. By combining numerical studies with experimental investigations to provide added physical insight and quantitative comparisons, shortcomings in the current model may be systematically addressed. With improvements, the current model may ultimately be used to determine the effect of process changes on macrosegregation in DC cast ingots and to develop control strategies for limiting macrosegregation during the casting process.

Acknowledgements

The authors would like to thank the Department of Energy for support of this research through Award Number DE-FG02-87ER13759.

References

[1] C.J. Vreeman, M.J.M. Krane, F.P. Incropera, The effect of free-floating dendrites and convection on macrosegregation in direct chill cast aluminum alloys Part I. model development, International Journal of Heat and Mass Transfer 43 (2000).
[2] H. Yu, D.A. Granger, Macrosegregation in aluminum alloy ingot cast by the semicontinuous direct chill (DC) method, in: Aluminum Alloys — Their Physical and Mechanical Properties, EMAS, UK, 1986, pp. 17–29.
[3] M.G. Chu, J.E. Jacoby, Macrosegregation characteristics of commercial size aluminum alloy ingot cast by the direct chill method, in: C.M. Bickert (Ed.), Light Metals 1990, TMS, 1990, pp. 925–930.
[4] R.C. Dorward, D.J. Beerntsen, Effects of casting practice on macrosegregation and microstructure of 2024 alloy billet, in: C.M. Bickert (Ed.), Light Metals 1990, TMS, 1990, pp. 919–924.
[5] W.D. Bennon, F.P. Incropera, A continuum model for momentum, heat and species transport in binary solid–liquid phase change systems — I. Model formulation, International Journal of Heat and Mass Transfer 30 (1987) 2161–2170.
[6] J. Ni, F.P. Incropera, Extension of the continuum model for transport phenomena occurring during metal alloy solidification — I. The conservation equations, International Journal of Heat and Mass Transfer 38 (1995) 1271–1284.
[7] P.J. Prescott, F.P. Incropera, W.D. Bennon, Modeling of dendritic solidification systems: reassessment of the continuum momentum equation, International Journal of Heat and Mass Transfer 34 (1991) 2351–2358.
[8] E.A. Barnes, G.B. Brook (Eds.), Smithell's Metals Reference Handbook, 7th ed., Butterworth–Heinemann, Oxford, 1992, pp. 14.1–14.14.
[9] P. Ocansey, M.S. Bhat, D.R. Poirier, Permeability for liquid flow in the mushy zones of equiaxed castings, in: U. Mannweiler (Ed.), Light Metals 1994, TMS, 1994, pp. 807–812.
[10] W.D. Bennon, F.P. Incropera, Numerical analysis of binary solid–liquid phase change using a continuum model, Numerical Heat Transfer 13 (1988) 277–296.
[11] L. Katgerman, S.C. Flood, A.H. Langille, Modelling of DC casting of aluminum alloys, in: M. Bouchard, P. Tremblay (Eds.), Production, Refining, Fabrication and Recycling of Light Metals, Pergamon Press, New York, 1990, pp. 96–110.
[12] D.C. Weckmann, P. Niessen, A numerical simulation of the D.C. continuous casting process including nucleate boiling heat transfer, Metallurgical and Materials Transactions B 13B (1982) 593–602.
[13] G.U. Grun, I. Eick, D. Vogelsang, Optimal design of a distribution pan for level pour casting, in: J. Evans (Ed.), Light Metals 1995, TMS, 1995, pp. 1061–1069.
[14] E.D. Tarapore, Thermal modeling of dc continuous bil-

let casting, in: P.G. Campbell (Ed.), Light Metals 1989, TMS, 1989, pp. 875–880.
[15] S. Patankar, in: Numerical Heat Transfer and Fluid Flow, Hemisphere, New York, 1980, pp. 113–134.
[16] C.J. Vreeman, F.P. Incropera, Numerical discretization of species equation source terms in binary mixture models of solidification and their impact on macrosegregation in semi-continuous, direct chill casting systems, Numerical Heat Transfer, Part B: Fundamentals 36(1) (1999) 1–14.
[17] M.J.M. Krane, F.P. Incropera, A scaling analysis of the unidirectional solidification of a binary alloy, International Journal of Heat and Mass Transfer 39 (1996) 3567–3579.
[18] A.V. Reddy, C. Beckermann, Modeling of macrosegregation due to thermosolutal convection and contraction-driven flow in direct chill continuous casting of an Al–Cu round ingot, Metallurgical and Materials Transactions B 28B (1997) 479–489.
[19] B. Griepy, Y. Caron, Investigation in the effects of casting parameters on the extent of centerline macrosegregation in DC cast sheet ingots, in: E.L. Rooy (Ed.), Light Metals 1991, TMS, 1991, pp. 961–971.
[20] A.V. Reddy, C. Beckermann, Simulation of the effects of thermosolutal convection, shrinkage induced flow, and solid transport on macrosegregation and equiaxed grain size distribution in a DC continuous cast Al–Cu round ingot, in: V.R. Voller, S.P. Marsh, N. El-Kaddah (Eds.), Materials Processing in the Computer Age II, 1995, pp. 89–102.